RSC Advances

PAPER

View Article Online
View Journal | View Issue

Cite this: *RSC Adv.*, 2023, **13**, 6356

Polyoxometalate supported on a magnetic Fe_3O_4/MIL-88A rod-like nanocomposite as an adsorbent for the removal of ciprofloxacin, tetracycline and cationic organic dyes from aqueous solutions†

Mona Ashrafi and Saeed Farhadi *

In this work, a magnetic $H_3PW_{12}O_{40}/Fe_3O_4$/MIL-88A (Fe) rod-like nanocomposite as a stable and effective ternary adsorbent was fabricated by the hydrothermal method and utilized for the removal of ciprofloxacin (CIP), tetracycline (TC) and organic dyes from aqueous solution. Characterization of the magnetic nanocomposite was accomplished by FT-IR, XRD, Raman spectroscopy, SEM, EDX, TEM, VSM, BET specific surface area and zeta potential analyses. The influencing factors on the adsorption potency of the $H_3PW_{12}O_{40}/Fe_3O_4$/MIL-88A (Fe) rod-like nanocomposite including initial dye concentration, temperature and adsorbent dose were studied. The maximum adsorption capacities of $H_3PW_{12}O_{40}/Fe_3O_4$/MIL-88A (Fe) for TC and CIP were 370.37 mg g^{-1} and 333.33 mg g^{-1} at 25 °C, respectively. In addition, the $H_3PW_{12}O_{40}/Fe_3O_4$/MIL-88A (Fe) adsorbent had high regeneration and reusability capacity after four cycles. In addition, the adsorbent was recovered through magnetic decantation and reused for three consecutive cycles without a considerable reduction in its performance. The adsorption mechanism was mainly ascribed to electrostatic and π–π interactions. According to these results, $H_3PW_{12}O_{40}/Fe_3O_4$/MIL-88A (Fe) can act as a reusable effective adsorbent for the fast elimination of tetracycline (TC), ciprofloxacin (CIP) and cationic dyes from aqueous solutions.

Received 10th December 2022
Accepted 17th February 2023

DOI: 10.1039/d2ra07898h

rsc.li/rsc-advances

1. Introduction

The rapid development of industrialization, has led to an increasing number of water pollutants such as dyes and antibiotics entering the environment. Organic dyes are a potential hazard to human health due to their various harmful effects.[1–4] The most important sources of industrial dye pollutants originate from different industries such as the textile, cosmetic, leather, food, pharmaceutical, paint and varnish, and pulp and paper industries.[5–8] Antibiotics play a major role in human and animal disease treatment, growth promotion, and prophylaxis.[9,10] Antibiotic pollution is becoming a serious problem. The main source of this contamination in the aquatic environment is wastewater from antibiotic manufacturers, large scale animal farming, and hospitals.[11] Tetracycline (TC), which belongs to polyketides has broad-spectrum antibacterial activities against various disease-causing pathogens.[12] Ciprofloxacin (CIP) is a type of antibiotic that is derived from the fluoroquinolones family, and used for healing the contagions induced by Gram-positive and Gram-negative bacteria.[13] However, extensive use of antibiotics has resulted in their frequent detection in the effluents of wastewater treatment plants (WWTPs). The incomplete metabolism of humans or animals and the undesirable removal performance of traditional technologies caused the residual CIP and TC to be continuously discharged into the natural water. There are many methods to remove cationic dyes, CIP, and TC, such as electrochemical purification, membrane processes.[14,15] biodegradation, and adsorption process using new adsorbents such as MOFs and Mxenes to remove different types of antibiotics and dyes.[16–18] Adsorption is widely used as an excellent and promising technique due to the great advantages which are based on its lower expenses, higher performance, and convenience in use.[19–21]

Polyoxometalates (POMs) are a big group of metal–oxygen clusters having acid–base properties, consisting of primary transition metals such as tungsten, vanadium, and molybdenum.[22,23] POMs are significant metal-oxide clusters with a highly negative charge and abundant topologies, which have been employed in many research fields such as optics, magnetism, catalysis, and biological medicine.[24,25] However, there are some disadvantages for the use of POMs as adsorbents: (1) their relatively small surface area seriously obstructs accessibility to the active sites and (2) their excellent solubility in aqueous solution determines that they cannot be reused and recycled in

Department of Inorganic Chemistry, Lorestan University, Khorramabad, 68151-44316, Iran. E-mail: farhadi.s@lu.ac.ir

† Electronic supplementary information (ESI) available. See DOI: https://doi.org/10.1039/d2ra07898h

the process of wastewater treatment. To solve these limitations, substrates including mof have been utilized to anchor polyoxometalates to the formation of heterogeneous composites.[26]

Metal–organic frameworks (MOFs) are hybrid crystalline porous materials with structures consisting of a regular array of positively charged metal ions or metallic clusters associated with organic linkers.[27] MOFs are porous materials with fascinating structures. The high surface area, crystallinity, controllable pore size, flexibility, and fictionalization of the porous surface are some of the main characteristics which determine the versatility of MOFs.[28,29] Among MOFs, one of the most attractive materials is MIL-88A (Fe). MIL-88A (Fe) was a 3D structured framework built up from trimers of Fe^{3+} octahedral linked to fumarate dianions. This structure exhibited a pore-channel system along the cages (5–7 Å).[30] Thus, these features make MIL-88A (Fe) to be a good candidate for environmental contaminant elimination.

Based on the above considerations, in this paper, a magnetic $H_3PW_{12}O_{40}/Fe_3O_4$/MIL-88A (Fe) rod-like nanocomposite was first fabricated by a hydrothermal method, and its chemical properties and physical structure were characterized. The adsorption of tetracycline (TC), ciprofloxacin (CIP), and organic dyes onto the $H_3PW_{12}O_{40}/Fe_3O_4$/MIL-88A (Fe) and the influences of the adsorbent dose, primary adsorbate concentration and temperature on the adsorption process were checked.

2. Experimental

2.1. Materials and procedures

Fumaric acid, iron(III) chloride ($FeCl_3 \cdot 6H_2O$, 99%), $H_3PW_{12}O_{40}$ (98%), ammonium iron(III) sulfate ($(NH_4)Fe(SO_4)_2 \cdot 12H_2O$, 98%), ammonium iron(II) sulfate ($(NH_4)_2Fe(SO_4)_2 \cdot 12H_2O$, 98.5%), ammonia NH_3, methylene blue ($C1_6H_{18}ClN_3S$, MB, 99%), methyl orange ($C_{14}H_{14}N_3NaO_3S$, MO, 99%), and rhodamine B ($C_{28}H_{31}ClN_2O_3$,RhB, 99%) were obtained from Merck company. Tetracycline ($C_{22}H_{24}N_2O_8$, TC, 99.5%) and ciprofloxacin ($C_{17}H_{18}FN_3O_3$, CIP, 95.5%) drugs were obtained from Exir pharmaceutic company (Boroujerd, Iran). All of the chemicals were used without further purification.

2.2. Synthesis of iron-based MIL-88A (Fe) nanorods

The sample of MIL-88A (Fe) was prepared through a hydrothermal procedure. The accurate action to the synthesis of iron-based MOF is as follows: $FeCl_3 \cdot 6H_2O$ (1.2 g) and fumaric acid (0.49 g) were poured into 25 mL Water and the obtained combine was stirred for 15 min at ambient temperature. The mixture within a 30 mL Teflon-lined autoclave was transferred and warmed for 12 h at 65 °C. Then, it was slowly cooled at 25 °C and the obtained light brown solid was separated through centrifugation. The solid result was washed with water and also with ethanol solvent three times. Eventually, the product was dried in an oven for 1 h at 60 °C.

2.3. Synthesis of magnetic Fe_3O_4/MIL-88A (Fe) nanorods

The Fe_3O_4/MIL-88A (Fe) nanocomposite was produced as follows: $FeCl_3 \cdot 6H_2O$ (1.2 g), fumaric acid (0.49 g), Fe_3O_4 (0.1 g), in 25 mL of water solvent was poured and the combine was stirred for 15 min at 25 °C. The mixture within a 30 mL Teflon-lined autoclave was transferred and warmed at 65 °C for 12 h. Afterward slowly cooled at 25 °C and the light brown solid product was separated the solid product was detached from the solution by applying a magnet and then washed with Water solvent and dried in an oven at 70 °C for 1 h.

2.4. Synthesis of $H_3P_2W_{12}O_{40}/Fe_3O_4$/MIL-88A (Fe) rod-like composite

For the fabrication of $H_3PW_{12}O_{40}/Fe_3O_4$/MIL-88A (Fe), 1 g of the Fe_3O_4/MIL-88A (Fe) and 1 g of $H_3PW_{12}O_{40}$ were solved within 20 mL of deionized water. The combine was stirred at 25 °C for 20 h. The resulting solid was washed through deionized water and cooled gradually at 25 °C. Finally, the solid product was detached from the solution by applying a magnet.

2.5. Characterization methods

FTIR spectra were registered with a Shimadzu-8400S spectrometer (Japan) in the wavenumber range of 400–4000 cm^{-1}. Powder XRD patterns were recorded by an X-ray diffractometer under a current of 40 mA and voltage of 40 kV with Cu Kα radiation ($k = 0.1542$ nm). The distribution and morphology of pure MOF and magnetic nanocomposite were studied utilizing (SEM, MIRA3 TESCAN) scanning electron microscopy connected with (EDX) energy-dispersive X-ray analysis. Spectra of UV-vis were performed on a Carry 100 Conc Varian spectrophotometer. The surface area of the nanocomposites was performed by N_2 adsorption isotherm with the BET method (Micro metrics PHS-1020, Japan). The magnetic (VSM) measurement was checked by MDKFD vibrating magnetometer (Daneshpajoohan Co., Iran) *via* a high magnetic field of 10 kOe. The adsorption process of dyes was measured on a Varian Cary 100 spectrophotometer (USA). Raman spectra were obtained using a Raman microscope (Senterra 2009, Germany) with a 514 nm line.

2.6. Adsorption experiments of drug

The adsorption of TC and CIP was performed in a 50 ml glass beaker and the adsorption reaction temperature was maintained at 25 °C. The removal experiments were carried out in 50 ml reaction volume of TC and CIP 10 mg L^{-1} and the parameters chosen for the optimization are nanoparticle concentration: 25–100 mg L^{-1} and temperature: 25–65 °C. After the reaction was completed, the adsorbent was separated with an external magnet. All parallel experiments were performed in triplicate to ensure accuracy, and the average results were employed for further data analysis. The main absorbance peak of TC and CIP was observed at 375 and 326 nm and its removal efficiency were calculated according to the following equation: The degradation efficiency (R (%)) is defined as $(C_o - C_t)/C_o \times 100\%$, where C_o is the initial concentration of TC and CIP solution and C_t is the remaining concentration of CIP at reaction time t.

$$R\ (\%) = (C_o - C_t) \times 100/C_o$$

and equilibrium adsorption capacity q_e (mg g^{-1}) could be computed:

$$q_e = (C_o - C_t) \times V/m$$

2.7. Adsorption experiments of organic dyes

The adsorption experiments were carried out using cationic dyes *i.e.*, MB, rhodamine B (RhB), and anionic dye, *i.e.*, methyl orange (MO) as model organic dye pollutants of the water at 25 ° C. In a typical experiment, 20 mg of the as-prepared $H_3PW_{12}O_{40}$/Fe_3O_4/MIL-88A (Fe), the hybrid adsorbent was added into 30 ml of dye aqueous solution with the initial concentration of 30 mg L^{-1} and stirred in the dark. The concentrations of MB, RhB, and MO were determined using UV-visible spectrophotometry at wavelengths of 664, 553, and 467 nm, respectively. The effects of important parameters on the adsorption performance, like amount of nanocomposite (10, 20, 30 and 40 mg) and initial dye concentration (25, 50, 75, 125, 150 and 200 mg), were studied under similar conditions as described above. To evaluate the selective adsorption ability of the hybrid nanomaterial, 20 mg of $H_3PW_{12}O_{40}/Fe_3O_4$/MIL-88A (Fe) was stirred with 30 ml of mixed dyes of MB + MO (C_o (MB) = C_o (MO) = 30 mg L^{-1}), MB + RhB (C_o (MB) = C_o (RhB) = 30 mg L^{-1}), MO + RhB (C_o (MB) = C_o (RhB) = 30 mg L^{-1}) and the ternary mixture of MB + MO + RhB (C_o (MB) = C_o (MO) = C_o (RhB) = 30 mg L^{-1}) and then the process was monitored using UV-visible spectroscopy at given time intervals. The elimination rate (R%) was computed based on the following equation:

$$(R\%) = (C_o - C_t) \times 100/C_o$$

3. Results and discussion

3.1. Characterization of the adsorbent

3.1.1. FTIR analysis. The FT-IR spectra of MIL-88A (Fe) (a), Fe_3O_4 (b), $H_3PW_{12}O_{40}$ (c), Fe_3O_4/MIL-88A (Fe) (d), and $H_3PW_{12}O_{40}/Fe_3O_4$/MIL-88A (Fe) rod-like composite (e) are displayed in Fig. 1. In Fig. 1(a), the broadband at about 3465 cm^{-1} is related to the stretching vibration of water molecules. The two sharp peaks at 1400 and 1610 cm^{-1} are assigned to symmetric and asymmetric vibrations of carboxyl groups, respectively, confirming the presence of the dicarboxylate linker within the sample.[31] Also, the peak that appeared at 574 cm^{-1} is specified to the Fe–O vibration. The FT-IR spectrum of Fe_3O_4 (Fig. 1(b)) demonstrated an adsorption peak at 567 cm^{-1} which is related to the vibration of the Fe–O bond of Fe_3O_4.[5] As revealed in Fig. 1(c), the characteristic peaks of 789 and 898 cm^{-1} are related to the vibration of (W–O_b–W), and the bands appeared at 960, and 1083 cm^{-1} are assigned to the vibrations of (W–O_d) and (P–O_a) of $H_3PW_{12}O_{40}$ polyanion, respectively.[32] Comparing the spectra of $H_3PW_{12}O_{40}/Fe_3O_4$/MIL-88A (Fe) samples (Fig. 1(d)) shows that after forming this nanocomposite, the characteristic peaks related to iron-based MIL-88A, $H_3PW_{12}O_{40}$, and Fe_3O_4 particles are slightly shifted. These shifts emphasize that a strong interaction exists between the $H_3PW_{12}O_{40}$ anion and Fe_3O_4 nanoparticles with MIL-88A (Fe) MOF.

3.1.2. XRD diffraction patterns. The crystallinity and phase of the fabricated samples MIL-88A (Fe), Fe_3O_4, $H_3PW_{12}O_{40}$, Fe_3O_4/MIL-88A (Fe), and $H_3PW_{12}O_{40}/Fe_3O_4$/MIL-88A (Fe) rod-like composite were analyzed *via* XRD as elucidated in Fig. 2. As shown in Fig. 2(a), the XRD pattern of MIL-88A showed two diffraction peaks at $2\theta = 10$–$12°$, which was accordance with the reported information.[31] As exhibited in Fig. 2(b), the typical peaks at $2\theta = 75°$, 63°, 53.7°, 43.3°, 36°, and 30.2° assigning to (440), (511), (422), (400), (311), and (220) the crystal planes of Fe_3O_4 particles (JCPDS card No. 19-0629).[33] In Fig. 2(c), the diffraction peaks of POM alone are observed. The XRD pattern of the nanocomposite sample in Fig. 2(d) exhibits the characteristic diffraction peaks corresponding to Fe_3O_4 and MIL-88A. Also, some diffraction peaks contributed to $H_3PW_{12}O_{40}$ phase are observed with low intensities because of the homogeneous distribution of the $H_3PW_{12}O_{40}$ molecules within the porous structure of MIL-88A (Fe). These findings confirm that the nanocomposite sample is composed of Fe_3O_4, MIL-88A and $H_3PW_{12}O_{40}$ components and it has been successfully prepared.[34]

3.1.3. Raman spectroscopy. Raman spectroscopy was used to confirm the structural phase of MIL-88A (Fe), $H_3PW_{12}O_{40}$, $H_3PW_{12}O_{40}$/MIL-88A (Fe), and $H_3PW_{12}O_{40}/Fe_3O_4$/MIL-88A (Fe) nanomaterials. In Fig. S1(a),† the bond of the fumaric acid molecule in MIL-88A was evidenced by the appearance of a band

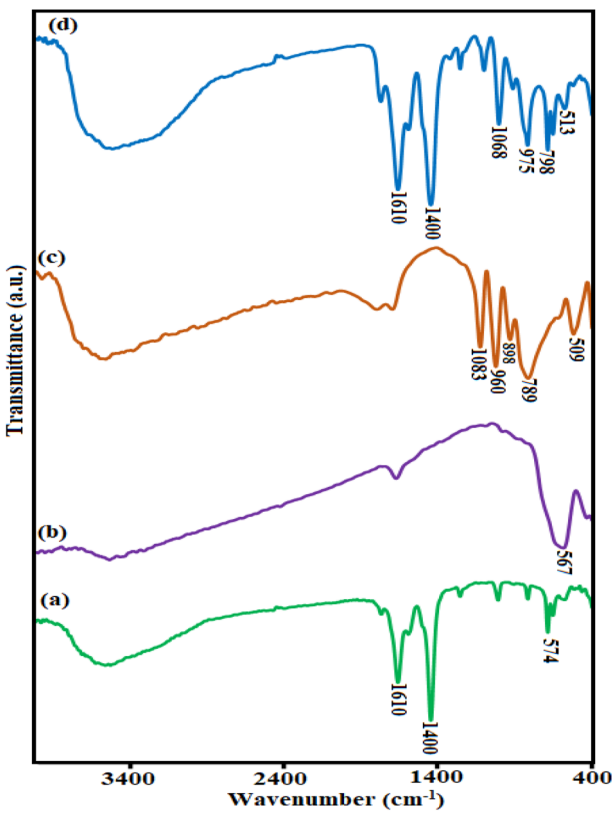

Fig. 1 The FTIR spectra of (a) MIL-88A (Fe), (b) Fe_3O_4, (c) $H_3PW_{12}O_{40}$, and (d) the $H_3PW_{12}O_{40}/Fe_3O_4$/MIL-88A Fe nanocomposite.

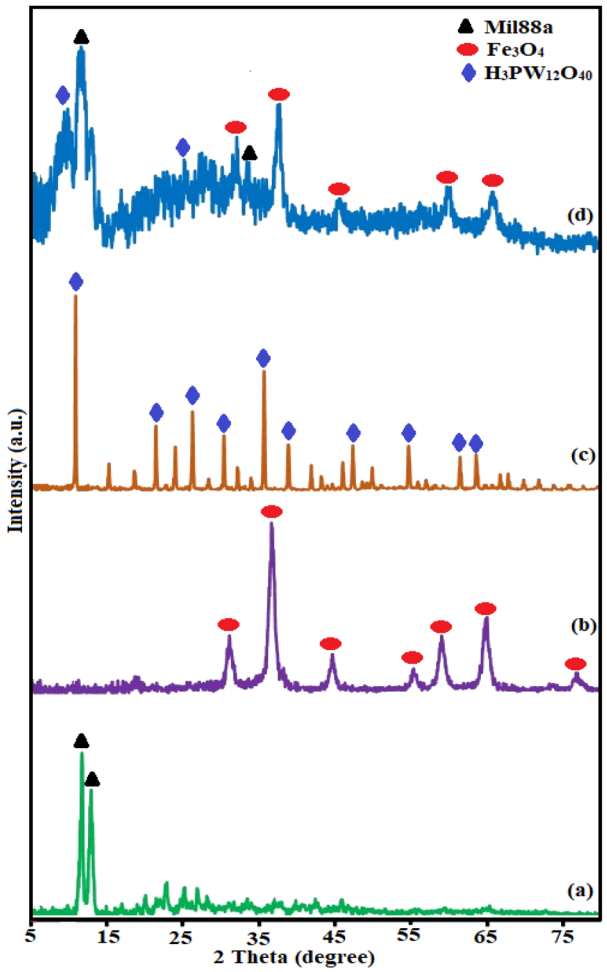

Fig. 2 The XRD patterns of (a) MIL-88A (Fe), (b) Fe_3O_4, (c) $H_3PW_{12}O_{40}$, and (d) the $H_3PW_{12}O_{40}/Fe_3O_4$/MIL-88A (Fe) nanocomposite.

at 3059 cm^{-1}, corresponding to the stretching sp^2 C–H vibrations, and a strong peak at 1649 cm^{-1} associated to the symmetric vibration modes C=C. The bands located at 1592 and 1435 cm^{-1}, in the case of MIL-88A, materials are attributed to the anti-symmetric and symmetric vibrations, respectively, of the carboxylate groups. The C–O bond was observed as an intense peak centered at 1280 cm^{-1}. Additionally, the bending vibrations outside the plane of the bond =C–H were placed at Raman shifts of 998, 896, and 763 cm^{-1}.[35] As exhibited in Fig. S1(b),† the Raman spectrum of $H_3PW_{12}O_{40}$ shows characteristic bands at 1010 cm^{-1} (stretching vibration of P–O), 990 cm^{-1} (stretching of W=O), 913 cm^{-1} (bending of W–O_c–W) and 519 cm^{-1} (bending of O–P–O). According to Fig. S1(c),† the appearance of some vibrational modes of the Fe_3O_4 and three bands of $H_3PW_{12}O_{40}$ at 292, 751, and 1010 cm^{-1}, beside the characteristic bands of MIL-88A (Fe), proved the existence of both Fe_3O_4 and $H_3PW_{12}O_{40}$ in the framework of MIL-88A (Fe).

3.1.4. SEM and TEM images. The morphology and microstructure of the iron-based MIL-88A (Fe), Fe_3O_4, Fe_3O_4/MIL-88A (Fe), and $H_3PW_{12}O_{40}/Fe_3O_4$/MIL-88A (Fe) samples were studied by utilizing SEM analyses as depicted in Fig. 3. According to Fig. 3(a) pure iron-based MIL-88a particles have a shape bar-like with two prismatic heads. In Fig. 3(b), the SEM image of Fe_3O_4 consists of small and near-spherical particles which is highly agglomerated. The SEM photographs of the binary Fe_3O_4/MIL-88A (Fe) (Fig. 3(c)) and ternary $H_3PW_{12}O_{40}/Fe_3O_4$/MIL-88A (Fe) nanocomposite (Fig. 3(d) and (e)) demonstrate that the morphology and shape of these samples are analogous to MIL-88A (Fe), which established that the framework of iron-based MIL-88A (Fe) remains unaltered after modification with Fe_3O_4 nanoparticles and $H_3PW_{12}O_{40}$. The morphology and microstructure of the as-prepared $H_3PW_{12}O_{40}/Fe_3O_4$/MIL-88A (Fe) nanocomposite were further investigated by TEM analysis. As evident from the image in Fig. 3(f), the morphology of the $H_3PW_{12}O_{40}/Fe_3O_4$/MIL-88A (Fe) rod-like composite sample from TEM images agreed with the SEM results.

3.1.5. EDX analysis. The EDX analysis of the $H_3PW_{12}O_{40}/Fe_3O_4$/MIL-88A (Fe) rod-like composite is displayed in Fig. S2.† In Fig. S2(a),† the EDX elemental spectrum of the ternary nanohybrid sample exhibits elemental peaks corresponding to $H_3PW_{12}O_{40}$ (O, P and W), Fe_3O_4 (Fe, O), and MIL-88A (Fe) (C, Cl, and Fe), with no other impure peaks observed, showing that the composite sample was composed of $H_3PW_{12}O_{40}$, Fe_3O_4, and MIL-88A (Fe). Further, the EDX elemental mappings of the composite in Fig. S2(b)† show the homogeneous dispersion of elements within the nanocomposite.

3.1.6. BET analysis. The N_2 adsorption–desorption isotherms of the activated MIL-88A (Fe) and $H_3PW_{12}O_{40}/Fe_3O_4$/MIL-88A (Fe) are illustrated in Fig. 4(a) and (b). The Brunauer–Emmett–Teller (BET) surface area values for MIL-88A (Fe) and $H_3PW_{12}O_{40}/Fe_3O_4$/MIL-88A (Fe) were calculated to be 3.19 $m^2\ g^{-1}$ and 4.16 $m^2\ g^{-1}$, respectively, in agreement with literature.[24] Their average pore diameter of them was measured as 41.2 nm and 47.4 nm, respectively. The BJH pore-size dispersions in the inset of the figures affirm the mesoporous cages of MIL-88A (Fe) and showed that the overall volume changes through the incorporation. The results suggested that the $H_3PW_{12}O_{40}$ polyoxometalate was mostly encapsulated within the channels and on the surface of MIL-88A (Fe).

3.1.7. VSM analysis. The magnetic properties of the pure Fe_3O_4, Fe_3O_4/MIL-88A (Fe), and $H_3PW_{12}O_{40}/Fe_3O_4$/MIL-88A (Fe) samples were investigated by VSM at room temperature, and the magnetic hysteresis loops are depicted in Fig. 5(a)–(c). The magnetic saturation values (M_s) of the Fe_3O_4 nanoparticles, Fe_3O_4/MIL-88A and $H_3PW_{12}O_{40}/Fe_3O_4$/MIL-88A (Fe) were about 72, 51 and 43 emu g^{-1}, respectively, which was sufficient for quick separation, *via* the aid of an outer magnet. This value was less than that of bare Fe_3O_4 (about 51 emu g^{-1}) because of the existence of nonmagnetic $H_3PW_{12}O_{40}$ and MIL-88A (Fe) components. The magnetic separability of the $H_3PW_{12}O_{40}/Fe_3O_4$/MIL-88A (Fe) nanocomposite was disclosed by approaching the glass container with a magnet.

3.1.8. Zeta potential analysis. The zeta potential investigation results got for analyzed MIL-88A (Fe) and $H_3PW_{12}O_{40}/Fe_3O_4$/MIL-88A (Fe) are presented in Fig. 6. As shown in Fig. 6, the positive zeta potential value of MIL-88A (Fe) (+4.59 mV) is changed to a negative charge for the $H_3PW_{12}O_{40}/Fe_3O_4$/MIL-88A

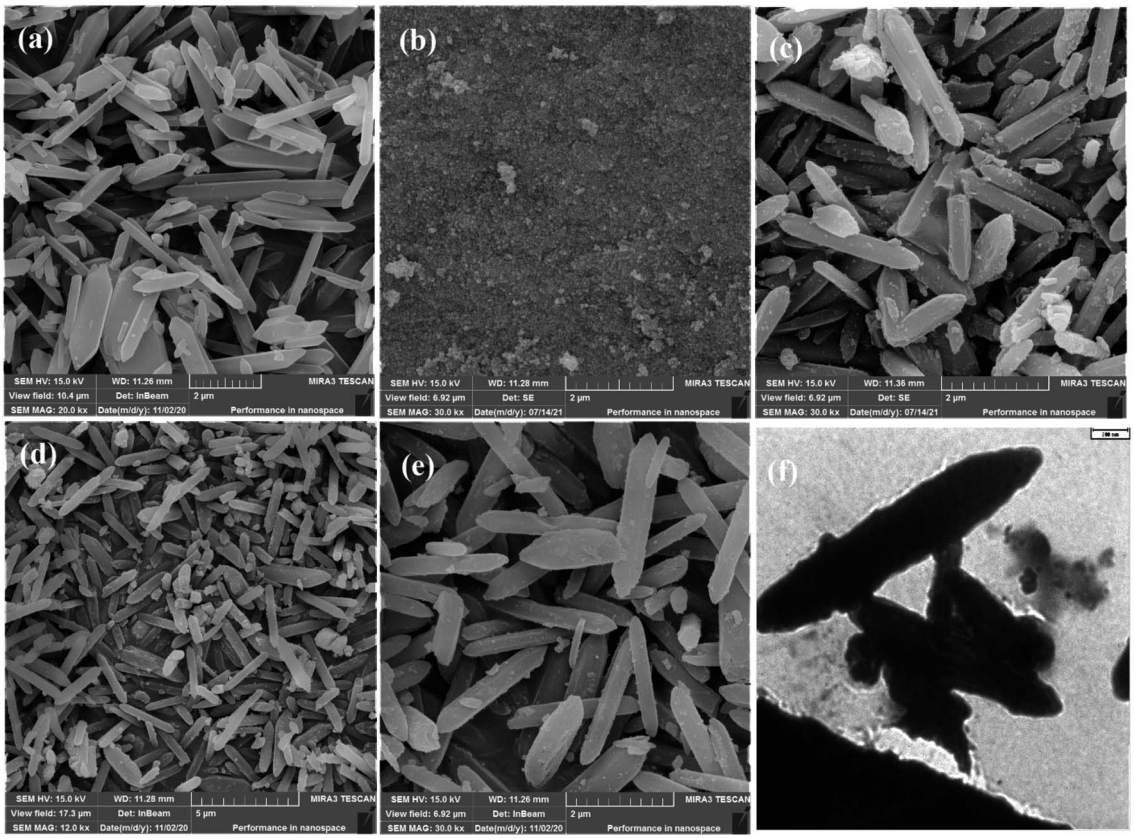

Fig. 3 The SEM photographs of (a) iron-based MIL-88A, (b) Fe_3O_4, (c) Fe_3O_4/MIL-88A (Fe), (d and e) the $H_3PW_{12}O_{40}/Fe_3O_4$/MIL-88A Fe nanocomposite, and (f) TEM image of the $H_3PW_{12}O_{40}/Fe_3O_4$/MIL-88A (Fe) nanocomposite.

(Fe) composite (−17.85 mV). This significant change in zeta potential value is mostly because of the introducing the negatively charged $PW_{12}O_{40}^{3-}$ component into the MIL-88A (Fe) framework and makes it more suitable for selective adsorption of cationic species.

3.2. TC and CIP drugs adsorption investigations

Different factors affect the adsorption process. The effect of $H_3PW_{12}O_{40}/Fe_3O_4$/MIL-88A (Fe) dosage, temperature and primary concentration of TC and CIP were investigated by a variable-controlling strategy. To determine the optimum adsorbent dosage, we explored the adsorbent effect on the TC and CIP removal efficiency. As shown in Fig. 7(a) and (b), the adsorption efficiency for TC is about 85% in 3 min and for CIP is approximately 100% in 12 min.

3.2.1. Influence of adsorbent dose. Different amounts of $H_3PW_{12}O_{40}/Fe_3O_4$/MIL-88A (Fe) nanocomposite (5, 10, 15, 20 mg) were added to investigate the influence of adsorbent dose on the CIP and TC removal efficiency. The results in Fig. 8(a) and (b) show that the removal efficiency increased with the nanocomposite dosage from 5 to 20 mg.[17,32] As expected, the removal (%) of drugs sharply increased with increasing the $H_3PW_{12}O_{40}/Fe_3O_4$/MIL-88A (Fe) nanocomposite composite dosage; this mainly attributed to the presence of further active sites for adsorption of drugs molecules. According to the above results, the amount of 10 mg was selected used for the subsequent adsorption experiments.

3.2.2. Influence of temperature. The adsorption behavior of $H_3PW_{12}O_{40}/Fe_3O_4$/MIL-88A (Fe) demonstrated at different temperatures in Fig. 9. As shown in Fig. 9(a), the progressive increase of temperature from 25 to 65 °C is adversely affecting the removal of 10 mg L^{-1} of TC by $H_3PW_{12}O_{40}/Fe_3O_4$/MIL-88A (Fe) nanocomposite, because the removal efficiency increase from 85% to 100%. This shows that the reaction between TC and $H_3PW_{12}O_{40}/Fe_3O_4$/MIL-88A (Fe) nanoparticles is the endothermic method. In Fig. 9(b), the influence of temperature on the elimination of CIP *via* $H_3PW_{12}O_{40}/Fe_3O_4$/MIL-88A (Fe) nanocomposite was checked at several temperatures from 25 to 65 °C under an adsorbent dosage of 10 mg. The results indicate that the adsorption process between ciprofloxacin and $H_3PW_{12}O_{40}/Fe_3O_4$/MIL-88A (Fe) nanoparticles is exothermic.[36,37]

3.2.3. Influence of primary TC and CIP concentration. The influence of the various initial concentrations (25, 50, 75, and 100 mg L^{-1}) of TC and CIP drugs on the adsorption efficiency of $H_3PW_{12}O_{40}/Fe_3O_4$/MIL-88A (Fe) adsorbent under the constant conditions of 50 mg L^{-1} absorbent, pH 6, and 25 °C are shown in Fig. 10. As can be seen in Fig. 10(a) and (b), the removal efficiency decreased with increasing the CIP and TC concentrations, probably due to the fast saturation of accessible active

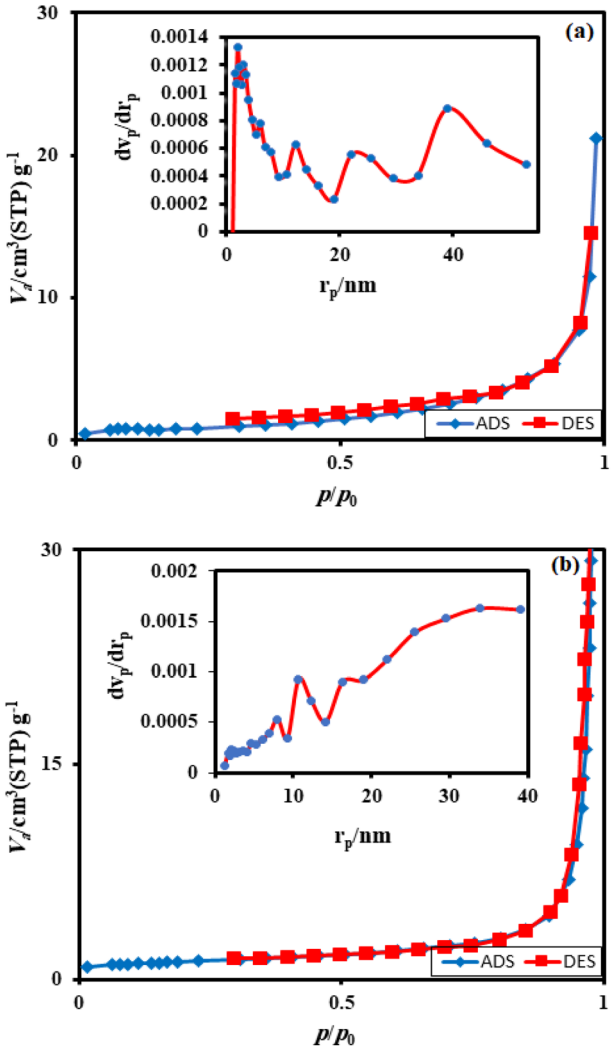

Fig. 4 N_2 adsorption–desorption isotherms and pore-size distribution curves (the insets) of (a) MIL-88A (Fe) and (b) the $H_3PW_{12}O_{40}/Fe_3O_4$/MIL-88A (Fe) nanocomposite.

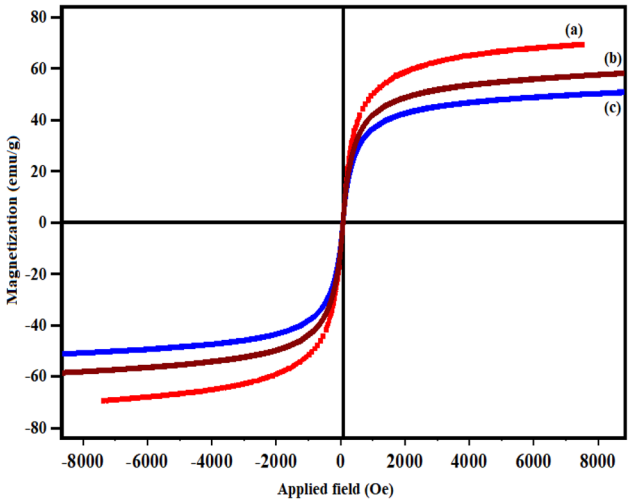

Fig. 5 Magnetization curves of (a) Fe_3O_4, (b) Fe_3O_4/MIL-88A (Fe) and (c) the $H_3PW_{12}O_{40}/Fe_3O_4$/MIL-88A (Fe) nanocomposite.

sites on the surface of adsorbent in higher initial concentration of drugs and the deficiency of active sites needed for high drug concentration.[32]

3.2.4. Removal efficiency of the nanocomposite components. The removal efficiency of pure MIL88A (Fe) and Fe_3O_4/MIL101 (Fe) in the elimination of TC and CIP from aqueous solutions were studied under the optimum reaction conditions in Fig. 11. The removal efficiency of these components into TC and CIP was 59–85% and 35–100% after adsorption times of 3–12 minutes and 12–24 minutes, respectively. The elimination percentage of the $H_3PW_{12}O_{40}/Fe_3O_4$/MIL-88A (Fe) nanocomposite is higher than the individual components and Fe_3O_4/MIL101 (Fe) composite, which showed the magnetic nanocomposite to be a better choice for the removal of the antibiotic drugs.

3.2.5. Comparison with some reported adsorbents. To indicate the advantage of the present adsorbent, we have compared the results in the removal of TC and CIP from aqueous solution by $H_3PW_{12}O_{40}/Fe_3O_4$/MIL-88A (Fe) nanocomposite with some reported similar adsorbents in the literature.[16,17,38–53] From Table 1, concerning the adsorption capacities, the present method is more suitable and/or superior. We can see that the adsorption process in the presence of some reported adsorbents demonstrated lower adsorption capacities compared to the present nanocomposite. The higher adsorption capacity of the $H_3PW_{12}O_{40}/Fe_3O_4$/MIL-88A (Fe) is the because of the synergistic effect between MIL-88A (Fe) and $H_3PW_{12}O_{40}$.

3.3. Dye adsorption investigations

To study and evaluate the absorption potential of $H_3PW_{12}O_{40}/Fe_3O_4$/MIL-88A (Fe) nanocomposite for the removal of dyes from contaminated waters, two organic dyes (MB and MO) with different charges were used for initial experiments. The adsorption was monitored using their special absorption bands, which are 664, and 463 nm for MB and MO, respectively. The time-dependent UV-visible absorption spectra of dyes in the presence of $H_3PW_{12}O_{40}/Fe_3O_4$/MIL-88A (Fe) are shown in Fig. 12. Fig. 12(a) and (b) shows that the characteristic absorption band of cationic MB dye at 664 nm almost completely disappeared within 6 min but the disappearance of band at about 463 nm for MO is almost negligible. This result shows that the nanocomposite is a poor absorbent for removing anionic MO dye from aqueous solution.

The selective uptake of dyes was investigated using the binary mixtures of MB + MO, MB + RhB, MO + RhB, and MB + MO + RhB with $H_3PW_{12}O_{40}/Fe_3O_4$/MIL-88A (Fe) as absorbent. As shown in Fig. 13(a) and (b), the preferable uptake of cationic MB and RhB dyes from the MB + MO and RhB + MO mixtures can be attributed to the anionic nature of $H_3PW_{12}O_{40}/Fe_3O_4$/MIL-88A (Fe). For further comparison, the binary mixture of cationic dyes (MB + RhB) was selected and the results in Fig. 13(c) revealed that MB and RhB were also adsorbed completely in the initial 3 min. As exhibited in

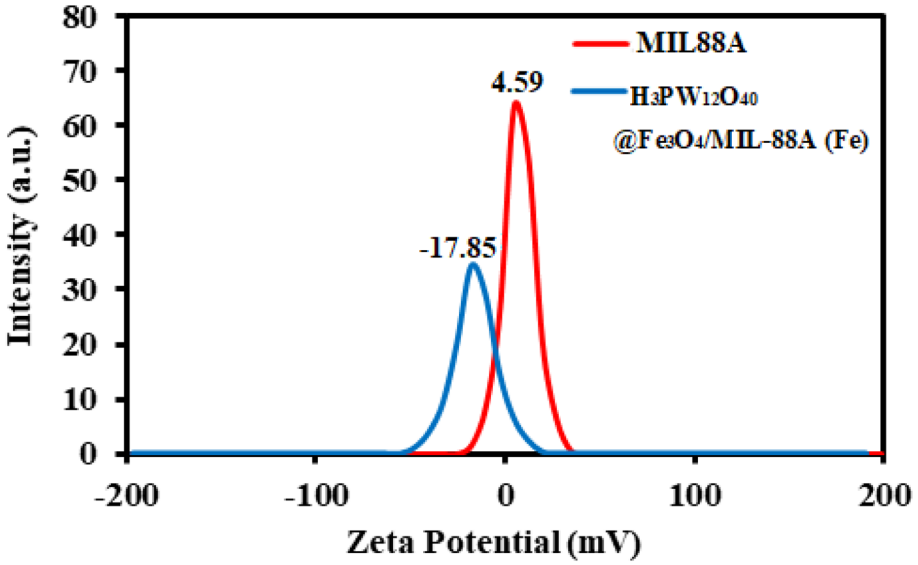

Fig. 6 Zeta potential distribution curve of the MIL-88A (Fe) and $H_3PW_{12}O_{40}/Fe_3O_4$/MIL-88A (Fe) samples in aqueous solutions.

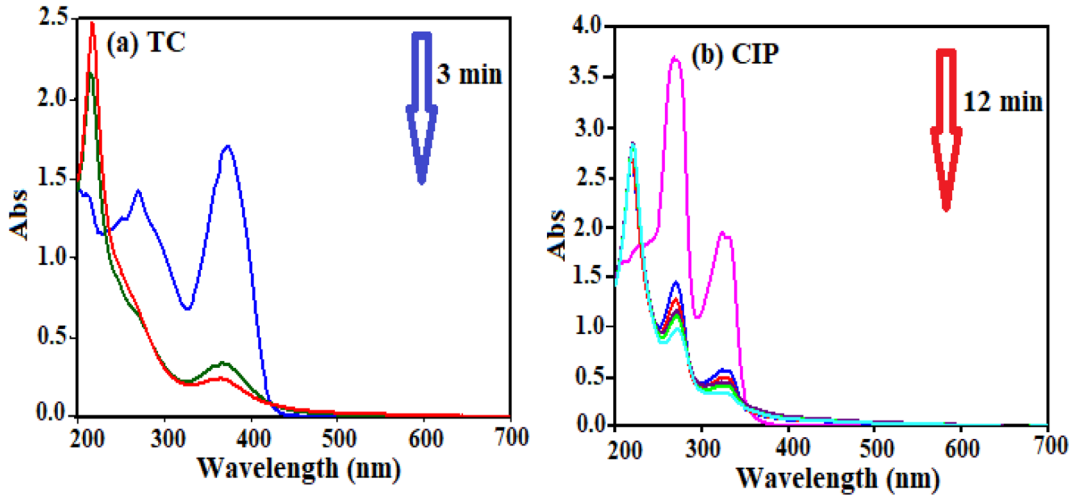

Fig. 7 UV-vis spectral changes of (a) TC and (b) CIP drugs in aqueous solutions over the $H_3PW_{12}O_{40}/Fe_3O_4$/MIL-88A (Fe) nanocomposite at different time intervals: conditions: C_o (drug) = 50 mg L^{-1}, V_{drug} = 50 mL, adsorbent dose: 10 mg at 25 °C.

Fig. 13(d), the representative peaks of MB + MO + RhB all disappeared quickly for the mixed dyes, and only the characteristic absorption peaks of MO remained, suggesting that $H_3PW_{12}O_{40}/Fe_3O_4$/MIL-88A (Fe) could selectively capture cationic dyes when utilized in the corresponding ternary mixture. This finding confirms that $H_3PW_{12}O_{40}/Fe_3O_4$/MIL-88A (Fe) nanocomposite also possesses selective adsorption ability towards cationic dyes in wastewater. So, the $H_3PW_{12}O_{40}/Fe_3O_4$/MIL-88A (Fe) nanocomposite exceptional adsorption properties towards the cationic MB and RhB molecules were clearly demonstrated. Some diverse effects on removal of colorants can be linked to the structure of the dye molecules and the nanocomposite as well. This is due to the existence of vastly electronegative $PW_{12}O_{40}^{3-}$, which mostly enhanced the adsorption ability of the porous material MIL-88A, which together with enormous numbers of negative charges may have a stronger force with the positive charges of the colorants. The fabricated material in this study is not an efficient adsorbent for the removal of MO, because of negative charges of both the adsorbent and dye molecules. As a consequence, there is neither electrostatic attraction nor adsorption property between the $PW_{12}O_{40}^{3-}$ encapsulated into the nanocomposite and MO molecules.

3.4. Possible adsorption mechanism

The behavior of TC and MB adsorption onto $H_3PW_{12}O_{40}/Fe_3O_4$/MIL-88A (Fe) were studied by the adsorbent properties,

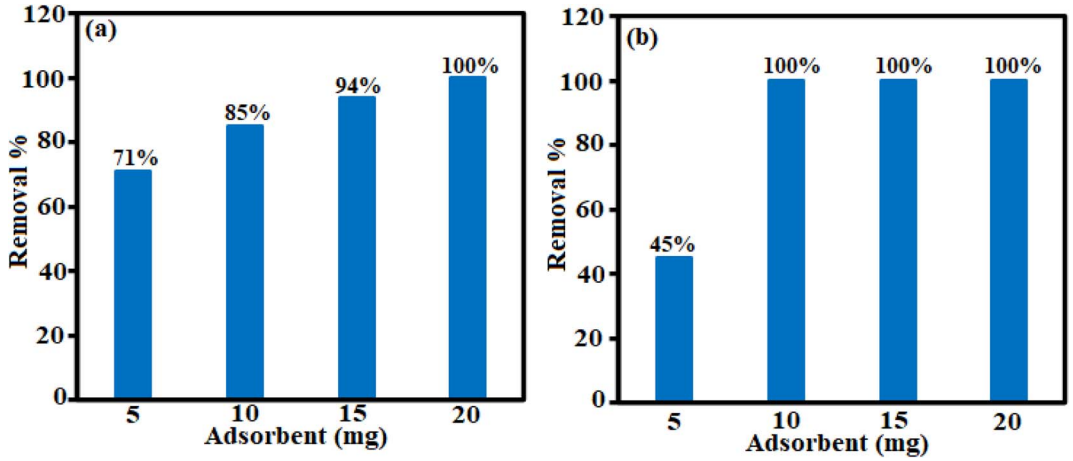

Fig. 8 Effect of adsorbent doses on the removal of (a) TC and (b) CIP antibiotics.

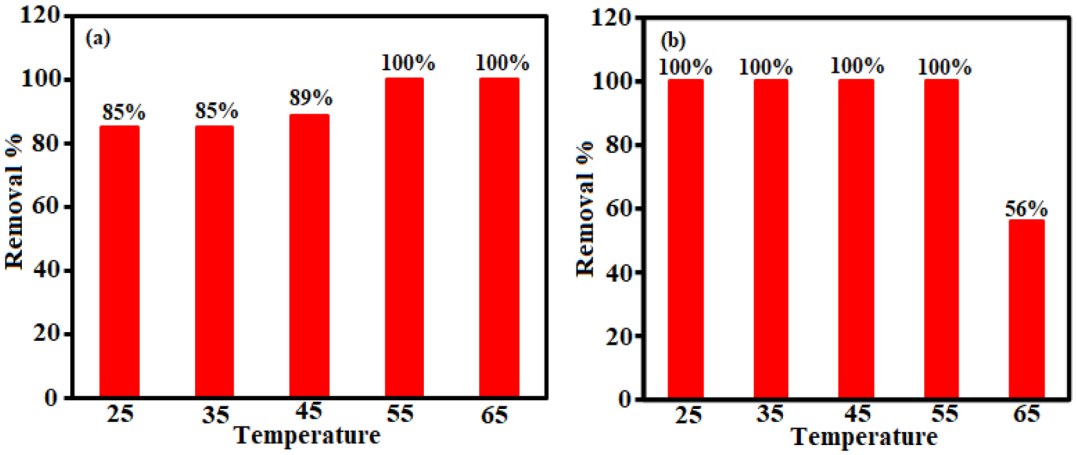

Fig. 9 Effects of temperature on the removal of (a) TC and (b) CIP antibiotics.

the TC and MB nature, electrostatic interaction, π–π interaction, hydrogen bonding, van der Waals, hydrophobic interaction sand surface complexation in this study. MB has a flat extended conjugated structure, which has stronger π–π stacking interactions compared to the TC. In addition, MB is a cationic dye, which exists as positively charged in an

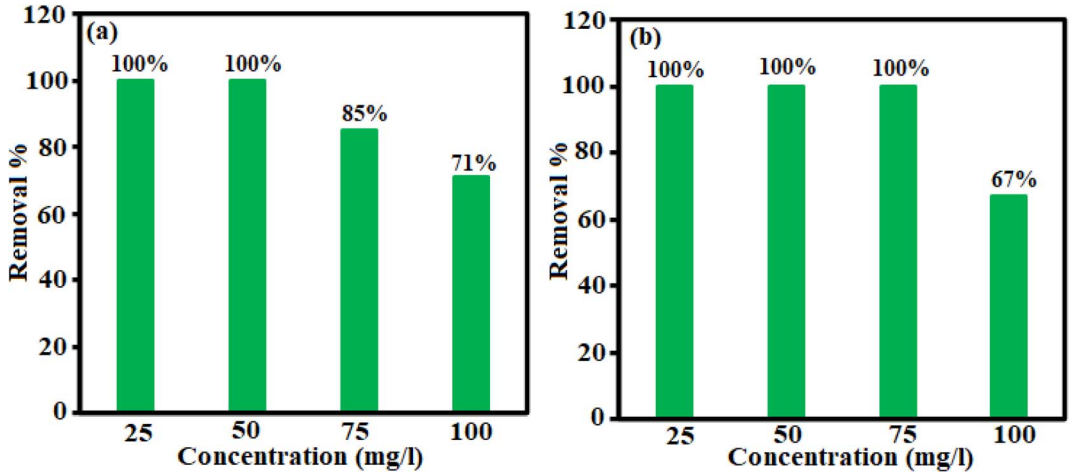

Fig. 10 Effect of concentration on the removal of (a) TC and (b) CIP antibiotics.

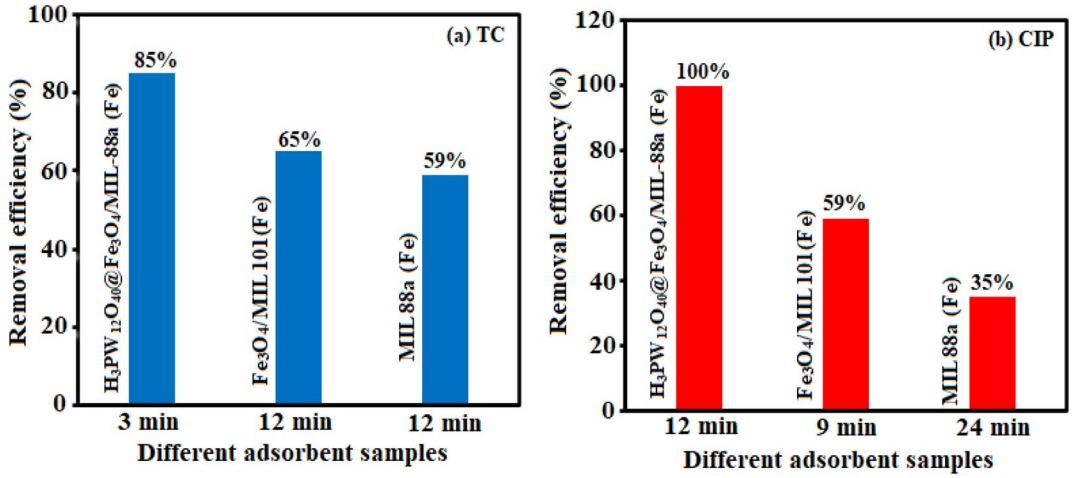

Fig. 11 The efficiency of the nanocomposite components on the removal of (a) TC and (b) CIP antibiotics.

Table 1 Comparison of the maximum adsorption capacities of some reported adsorbents for TC and CIP drugs

Adsorbent	Drug	Maximum adsorption capacity (mg g^{-1})	Ref.
HAP/MIL101 (Fe)/Fe_3O_4	CIP	112.35	16
Fe_3O_4/cellulose	CIP	6.90	17
Fe_3O_4/cellulose	CIP	168.03	17
CS-g-PA/TSM	CIP	238.3	38
MIL101 (Cr)–HSO_3	CIP	564.9	39
c-FD	CIP	328	40
mGOCP	CIP	283.44	41
Ga-cl-PAM/C_3N_4	CIP	169.49	42
Fe/Zn-SBC	CIP	74.2	43
Fe/Zn-SBC	TC	145	43
Fe_3O_4/MIL-53 (Al)–NH_2	TC	84.8	44
MnO_2/graphene	TC	195.31	45
Graphene oxide/ZnO	TC	159	46
Fe_3O_4@MIL-53 (Al)	TC	47.8	47
$MnFe_2O_4$/rGO	TC	41	48
Scallop shell coated Fe_2O_3 nanocomposite	TC	49.26	49
CTM/Fe_3O_4	TC	215.31	50
CDF/MF	TC	168.24	51
MWCNT/MIL-53 (Fe)	TC	180.68	52
CNT/$MnFe_2O_4$	TC	86.48	53
CNT/β-CD/$MnFe_2O_4$	TC	89.53	53
ZnAl-LDH/biochar	TC	41.98	54
$H_3PW_{12}O_{40}$/Fe_3O_4/MIL-88A (Fe)	TC	370.37	This work
$H_3PW_{12}O_{40}$/Fe_3O_4/MIL-88A (Fe)	CIP	333.33	This work

aqueous solution. The adsorption efficiency of the MIL-88A (Fe), sample, despite its higher surface area, was lower than that of the $H_3PW_{12}O_{40}$/Fe_3O_4/MIL-88A (Fe) composite. This confirms that other factors influence the adsorption efficiency besides to the specific surface area of the adsorbent. After introducing the $PW_{12}O_{40}^{3-}$ polyanions into the cavities of MIL-88A (Fe), it was confirmed that the adsorption capacity of the nanocomposite changed, in comparison with that of MIL-88A (Fe). This is because of the rapid and effective adsorption of cationic MB dye by $PW_{12}O_{40}^{3-}$ polyanions, whereas it is unfavorable for $H_3PW_{12}O_{40}$/Fe_3O_4/MIL-88A (Fe) to adsorb the anionic dye MO. These findings show that the $PW_{12}O_{40}^{3-}$ polyoxoanion clusters encapsulated in the mesoporous cages of MIL-88A (Fe) act as the active sites for the adsorption of cationic dye molecules. The zeta potential of a material is another key factor influencing its adsorption capacity; therefore, this was tested to understand further why the $H_3PW_{12}O_{40}$/Fe_3O_4/MIL-88A (Fe) sample can remove the cationic dyes MB more effectively than the anionic MO dye. The zeta potentials of MIL-88A (Fe) and $H_3PW_{12}O_{40}$/Fe_3O_4/MIL-88A (Fe) samples were measured as +4.59 and −17.85 mV, respectively, in water at natural pH. After modification with $H_3PW_{12}O_{40}$, the $H_3PW_{12}O_{40}$/Fe_3O_4/MIL-88A (Fe) nanocomposite showed a more negative zeta potential than the pristine MIL-88A (Fe) sample, thus, it can adsorb more of the cationic dyes such as MB, whereas it is unfavorable to adsorb the anionic dyes such as MO.

Also in this work, the adsorption efficiency of $H_3PW_{12}O_{40}$/Fe_3O_4/MIL-88A (Fe) was found to be higher as compared to pure $H_3PW_{12}O_{40}$, MIL-88A (Fe), and Fe_3O_4/MIL-88A (Fe). First, there are many open metal sites on MIL-88A (Fe) that facilitate the adsorption of specific guest molecules with corresponding functional groups.[55,56] Since the adsorption could happen inside the MOFs, hydrogen bonding may also occur during the tetracycline adsorption process. TC molecule has a complex structure with several carbonyls, amino and hydroxyl functional groups, and O-containing groups of the $H_3PW_{12}O_{40}$/Fe_3O_4/MIL-88A (Fe) composite such as OH, NH_2 and carboxylate.[57] The aromatic structure of the drugs molecule adsorption onto MIL-88A (Fe), series mainly occurred by π–π interaction. The O-containing groups in MIL-88A (Fe) and $PW_{12}O_{40}^{3-}$ play an important role in the adsorption process.[58] The reason for high adsorption of TC and MB on samples should be further investigated.

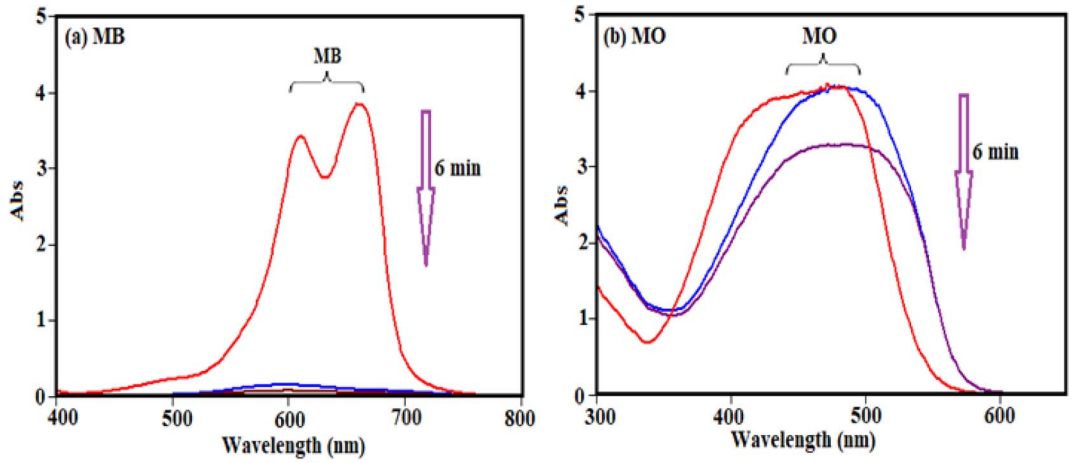

Fig. 12 The UV-vis spectra during adsorption of (a) cationic MB and (b) anionic MO dyes over the $H_3PW_{12}O_{40}/Fe_3O_4$/MIL-88A (Fe): C_o (dye) = 30 mg L^{-1}, V_{dye} = 30 mL, adsorbent dosage = 20 mg, temp = 25 °C.

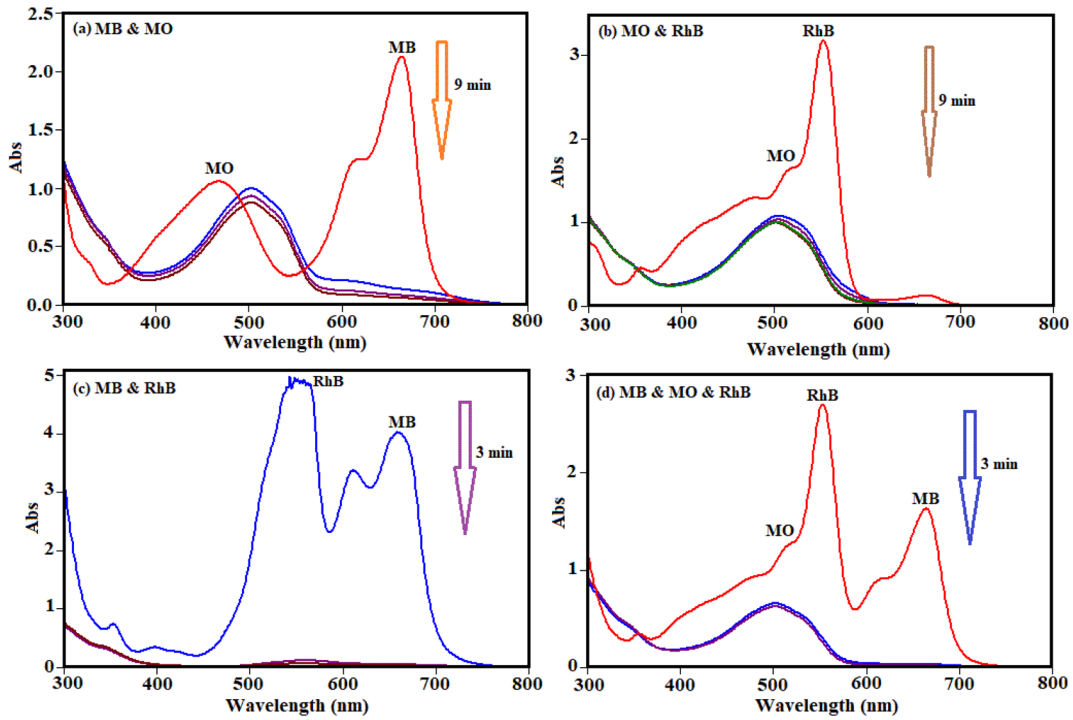

Fig. 13 Selective adsorption capability of $H_3PW_{12}O_{40}/Fe_3O_4$/MIL-88A (Fe) into the combined solution of (a) MB + MO, (b) MB + RhB, (c) MO + RhB, and (d) MB + MO + RhB. Conditions: C_o (MB) = C_o (RhB) = C_o (MO) = 35 mg L^{-1}, and adsorbent dosage = 20 mg in 30 mL.

3.5. Stability and reusability of the magnetic nanocomposite

To check the reusability of the $H_3PW_{12}O_{40}/Fe_3O_4$/MIL-88A (Fe) as an adsorbent, cycle experiments were carried out by applying a combination of methanol and deionized water as desorption solvents. For this goal, 10 mg of nanocomposite was added in TC and CIP solutions with a concentration of 50 mg L^{-1}, and stirred for 30 minutes, in continuing the nanocomposite was thoroughly detached by utilizing a magnet. In the next, the magnetic nanocomposite was eluted with a methanol solution several times and finally dried for 12 h at 25 °C and reused for another adsorption process under the same condition. The results in Fig. 14(a) show the adsorbent is reusable for at minimum 3 runs without notable loss of activity. As indicated in Fig. 14 (b)–(d), SEM, FT-IR, and XRD analyses of the recycled $H_3PW_{12}O_{40}/Fe_3O_4$/MIL-88A (Fe) after 4 runs were identical to the fresh nanocomposite. These results established that the structure of the magnetic nanocomposite was stable and was not altered by the reactants.

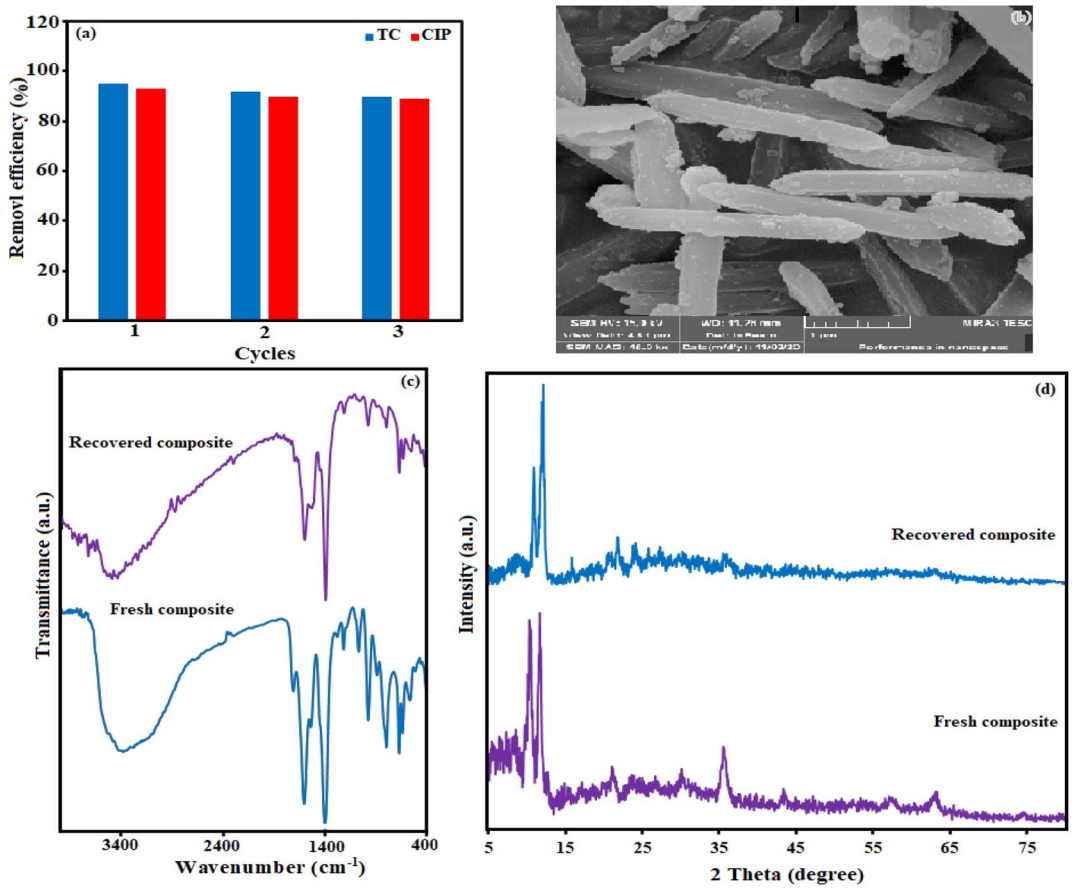

Fig. 14 (a) Reusability of the $H_3PW_{12}O_{40}/Fe_3O_4$/MIL-88A (Fe) nanocomposite in the removal of TC and CIP antibiotics, (b) SEM image, (c) FT-IR spectrum and (d) XRD pattern of the fresh and recovered nanocomposite after three runs.

4. Conclusions

In summary, a magnetically separable $H_3PW_{12}O_{40}/Fe_3O_4$/MIL-88A (Fe) adsorbent was successfully prepared using a hydrothermal method and its adsorptive property of organic dyes and antibiotics entering the environment were investigated. The tests showed that the magnetic nanocomposite $H_3PW_{12}O_{40}/Fe_3O_4$/MIL-88A (Fe) offers high removal efficiency against cationic dyes, TC, and CIP antibiotics. The maximum adsorption capacities of TC and CIP drugs onto $H_3PW_{12}O_{40}/Fe_3O_4$/MIL-88A (Fe) composite were found to be 370.33 and 333.33 mg g^{-1}, respectively. Also, reusability tests showed that $H_3PW_{12}O_{40}/Fe_3O_4$/MIL-88A (Fe) composite can be reused for three cycles without a considerable reduction in its performance. As a result, magnetic nanocomposite could be used as an efficient to remove cationic dyes antibiotics from water.

Conflicts of interest

There are no conflicts to declare.

Acknowledgements

The authors give their sincere thanks to the Lorestan University and Iran Nanotechnology Initiative Council (INIC) for all provided supports.

References

1 R. Hajavazzadeh, M. Kargar Razi and A. R. Mahjoub, *Int. J. Nano Dimens.*, 2021, **12**, 67–75.
2 A. Golshan Tafti, A. Rashidi, H.-A. Tayebi and M. E. Yazdanshenas, *Int. J. Nano Dimens.*, 2018, **9**, 79–88.
3 S. Ahmadi, L. Mohammadi, A. Rahdar, S. Rahdar, R. Dehghani, C. Adaobi Igwegbe and G. Z. Kyzas, *Nanomaterials*, 2020, **10**, 556.
4 S. Rahdar, A. Rahdar, M. N. Zafar, S. S. Shafqat and S. Ahmadi, *J. Mater. Res. Technol.*, 2019, **8**, 3800–3810.
5 A. Jarrah and S. Farhadi, *J. Solid State Chem.*, 2020, **285**, 121264.
6 L. Zhu, L. Zong, X. Wu, M. Li, H. Wang, J. You and C. Li, *ACS Nano*, 2018, **12**, 4462–4468.
7 Z. Wang, L. Song, Y. Wang, X.-F. Zhang and J. Yao, *J. Phys. Chem. Solids*, 2021, **150**, 109839.
8 M. Fayazi, D. Afzali, R. Ghanei-Motlagh and A. Iraji, *Environ. Sci. Pollut.*, 2019, **26**, 18893–18903.
9 X. Song, J. Mo, Y. Fang, S. Luo, J. Xu and X. Wang, *Environ. Sci. Pollut.*, 2022, **29**, 35204–35216.
10 G. Gopal, H. Sankar, C. Natarajan and A. Mukherjee, *J. Environ. Manage.*, 2020, **254**, 109812.
11 C. Liu, L. Tan, L. Zhang, W. Tian and L. Ma, *Front. Environ. Sci.*, 2021, **9**, 692298.

12 Y. Zhang, Z. Jiao, Y. Hu, S. Lv, H. Fan, Y. Zeng, J. Hu and M. Wang, *Environ. Sci. Pollut.*, 2017, **24**, 2987–2995.
13 N. A. Elessawy, M. Elnouby, M. H. Gouda, H. A. Hamad, N. A. Taha, M. Gouda and M. S. M. Eldin, *Chemosphere*, 2020, **239**, 124728.
14 Z. Liu, M. Zhu, L. Zhao, C. Deng, J. Ma, Z. Wang, H. Liu and H. Wang, *Chem. Eng. J.*, 2017, **314**, 59–68.
15 X. Liu, D. Yang, Y. Zhou, J. Zhang, L. Luo, S. Meng, S. Chen, M. Tan, Z. Li and L. Tang, *Chemosphere*, 2017, **182**, 306–315.
16 M. Beiranvand, S. Farhadi and A. Mohammadi-Gholami, *RSC Adv.*, 2022, **12**, 34438–34453.
17 A. Azizi, *J. Iran. Chem. Soc.*, 2021, **18**, 331–341.
18 L. Zhang, P. Ma, L. Dai, S. Li, W. Yu and J. Guan, *Catal. Sci. Technol.*, 2021, **11**, 3834–3844.
19 M. Martínez-Cabanas, M. Lopez-Garcia, J. L. Barriada, R. Herrero and M. E. S. de Vicente, *Chem. Eng. J.*, 2016, **301**, 83–91.
20 J. Yang, Q. Xiao, X. Jia, Y. Li, S. Wang and H. Song, *J. Hazard. Mater.*, 2021, **403**, 124016.
21 W. Wang, W. Zhao, H. Zhang, J. Xu, L. Zong, Y. Kang and A. Wang, *Powder Technol.*, 2021, **390**, 303–314.
22 N. I. Gumerova and A. Rompel, *Nat. Rev. Chem.*, 2018, **2**, 1–20.
23 O. R. Tambunan and R. Mohadi, *J. Sci. Technol.*, 2017, **2**, 1–8.
24 N. A. Ramsahye, T. K. Trung, L. Scott, F. Nouar, T. Devic, P. Horcajada, E. Magnier, O. David, C. Serre and P. Trens, *Chem. Mater.*, 2013, **25**, 479–488.
25 S. M. Wang, J. Hwang and E. Kim, *J. Mater. Chem.*, 2019, **7**, 7828–7850.
26 C. T. Buru, P. Li, B. L. Mehdi, A. Dohnalkova, A. E. Platero-Prats, N. D. Browning, K. W. Chapman, J. T. Hupp and O. K. Farha, *Chem. Mater.*, 2017, **29**, 5174–5181.
27 A. M. Andani, T. Tabatabaie, S. Farhadi and B. Ramavandi, *RSC Adv.*, 2020, **10**, 32845–32855.
28 F. Mahmoudi and M. M. Amini, *J. Water Proc. Eng.*, 2020, **35**, 101227.
29 R. Narayan, U. Y. Nayak, A. M. Raichur and S. Garg, *Pharmaceutics*, 2018, **10**(1–49), 118.
30 A. Benítez, J. Amaro-Gahete, D. Esquivel, F. J. Romero-Salguero, J. Morales and Á. Caballero, *Nanomaterials*, 2020, **10**, 424.
31 V. P. Viswanathan, K. Divya, D. P. Dubal, N. N. Adarsh and S. Mathew, *Dalton Trans.*, 2021, **50**, 2891–2902.
32 A. Jarrah and S. Farhadi, *RSC Adv.*, 2018, **8**, 37976–37992.
33 T. Wang, P. Zhao, N. Lu, H. Chen, C. Zhang and X. Hou, *Chem. Eng. J.*, 2016, **295**, 403–413.
34 J. Wu, S. Jin, X. Wei, F. Gu, Q. Han, Y. Lan, C. Qian, J. Li, X. Wang and R. Zhang, *Chem. Eng.*, 2021, **412**, 128712.
35 A. Benítez de la Torre, J. Amaro-Gahete, D. Esquivel, F. J. Romero-Salguero, J. Morales and Á. Caballero, *Nanomaterials*, 2020, **10**, 424.
36 Y. Yue, Z. Peng, W. Wang, Y. Cai, F. Tan, X. Wang and X. Qiao, *Powder Technol.*, 2019, **347**, 1–9.
37 Y. X. Song, S. Chen, N. You, H. T. Fan and L. N. Sun, *Chemosphere*, 2020, **255**, 126917.
38 Y. K. Manea, A. M. Khan, A. A. Wani, M. T. Qashqoosh, M. Shahadat and M. A. Salem, *J. Mol. Liq.*, 2021, **335**, 116144.
39 Z. Li, M. Ma, S. Zhang, Z. Zhang, L. Zhou, J. Yun and R. Liu, *J. Porous Mater.*, 2020, **27**, 189–204.
40 A. Jain, A. Sharma, A. Kapur, S. Wadhawan, M. Garg, S. K. Pandey, S. Singh and S. K. Mehta, *J. Nanostruct. Chem.*, 2021, **11**, 437–453.
41 Y. Zhou, S. Cao, C. Xi, X. Li, L. Zhang, G. Wang and Z. Chen, *Bioresour. Technol.*, 2019, **292**, 121951.
42 G. Sharma, B. Thakur, A. Kumar, S. Sharma, M. Naushad and F. J. Stadler, *Macromol. Mater. Eng.*, 2020, **305**, 2000274.
43 Y. Ma, M. Li, P. Li, L. Yang, L. Wu, F. Gao, X. Qi and Z. Zhang, *Bioresour. Technol.*, 2021, **319**, 124199.
44 G. Zhang, R. Wo, Z. Sun, L. Xiao, G. Liu, G. Hao, H. Guo and W. Jiang, *Front. Chem.*, 2021, **9**, 707559.
45 Z. Song, Y. L. Ma and C. E. Li, *Sci. Total Environ.*, 2019, **651**, 580–590.
46 D. Qiao, Z. Li, J. Duan and X. He, *Chem. Eng. J.*, 2020, **400**, 125952.
47 H. Molavi, H. Moghimi and R. A. Taheri, *Appl. Organomet. Chem.*, 2020, **34**, e5549.
48 J. Bao, Y. Zhu, S. Yuan, F. Wang, H. Tang, Z. Bao, H. Zhou and Y. Chen, *Nanoscale Res. Lett.*, 2018, **13**, 396.
49 D. Naghipour, K. Taghavi, J. Jaafari, I. Kabdaşlı, M. Makkiabadi, M. Javan Mahjoub Doust and F. Javan Mahjoub Doust, *Environ. Technol.*, 2023, **44**, 150–160.
50 T. Ahamad, M. Naushad, T. Al-Shahrani, N. Al-Hokbany and S. M. Alshehri, *Int. J. Biol. Macromol.*, 2020, **147**, 258–267.
51 T. Ahamad, A. A. Chaudhary, M. Naushad and S. M. Alshehri, *Int. J. Biol. Macromol.*, 2019, **134**, 180–188.
52 W. Xiong, G. Zeng, Z. Yang, Y. Zhou, C. Zhang, M. Cheng, Y. Liu, L. Hu, J. Wan, C. Zhou, R. Xu and X. Li, *Sci. Total Environ.*, 2018, **627**, 235–244.
53 R. Foroutan, S. J. Peighambardoust, P. Latifi, A. Ahmadi, M. Alizadeh and B. Ramavandi, *J. Environ. Chem.*, 2021, **9**, 106344.
54 L. P. Hoang, T. M. P. Nguyen, H. T. Van, M. Yılmaz, T. K. Hoang, Q. T. Nguyen, T. M. H. Vi and L. T. Q. Nga, *Environ. Technol. Innovation*, 2022, **28**, 102914.
55 Y. Sun, M. Chen, H. Liu, Y. Zhu, D. Wang and M. Yan, *Appl. Surf. Sci.*, 2020, **525**, 146614.
56 J. Yu, W. Xiong, X. Li, Z. Yang, J. Cao, M. Jia, R. Xu and Y. Zhang, *Microporous Mesoporous Mater.*, 2019, **290**, 109642.
57 X. Zhang, X. Lin, Y. He and X. Luo, *Int. J. Biol. Macromol.*, 2019, **136**, 445–459.
58 N. Tian, Q. Jia, H. Su, Y. Zhi, A. Ma, J. Wu and S. Shan, *J. Porous Mater.*, 2016, **23**, 1269–1278.